



# On the Hemispheric Bias Seen in Vector Magnetic Field Data

Yang Liu<sup>1</sup> · Ana Belén Griñón-Marín<sup>1,2,3</sup> · Jon T. Hoeksema<sup>1</sup> · Aimee A. Norton<sup>1</sup> · Xudong Sun<sup>4</sup>

Received: 16 September 2021 / Accepted: 5 January 2022 / Published online: 27 January 2022  
© The Author(s), under exclusive licence to Springer Nature B.V. 2022

## Abstract

The east–west component of the magnetic field,  $B_\phi$ , as observed in solar magnetograms containing quiet regions, is found to change its sign when the regions cross the central meridian. It is seen in both HMI/SDO and VSM/SOLIS full disk vector magnetograms. A mismatch between the calibrated line-of-sight and transverse fields is the reason for this hemispheric bias problem. Here mismatch means that one of the fields is either over-estimated or under-estimated. For HMI data, the transverse field is over-estimated. This mismatch is caused ultimately by a filling factor that is not precisely determined when unresolved structures are present. An updated inversion procedure for HMI observations, developed recently, is able to derive the filling factor with reasonable accuracy. The new data show that the hemispheric bias problem has been mitigated substantially.

**Keywords** Instrumentation and data management · Magnetic fields, photosphere

## 1. Introduction

Solar eruptions are one of the main causes that lead to geoeffective events, and thus sometimes greatly impact the Earth's environment. Understanding and predicting such eruptions is one of the essential goals in the solar physics community.

It is generally accepted that solar magnetic fields drive the eruptions and that the energy stored in the fields is the main driver of the eruptions. Thus, measuring solar magnetic fields is important for understanding solar eruptions and geoeffective events. Not only can measured magnetic fields provide information on the structure and evolution of solar magnetic fields to study the mechanisms of eruption, but also drive numerical simulations to understand and forecast solar events.

---

✉ Y. Liu  
[yliu@sun.stanford.edu](mailto:yliu@sun.stanford.edu)

<sup>1</sup> W. W. Hansen Experimental Physics Laboratory, Stanford University, Stanford, CA 94305-4085, USA

<sup>2</sup> Institute of Theoretical Astrophysics, University of Oslo, P.O. Box 1029 Blindern, 0315 Oslo, Norway

<sup>3</sup> Rosseland Centre for Solar Physics, University of Oslo, P.O. Box 1029 Blindern, 0315 Oslo, Norway

<sup>4</sup> Institute for Astronomy, University of Hawai'i at Mānoa, Pukalani, HI 96768, USA

The Sun's magnetic field has been measured for many years. Most observations in the past were taken routinely with a limited field of view for vector magnetic field measurement, or only one component, the line-of-sight field for the entire disk of the Sun. The full disk vector magnetic field observations were routinely made after 2003 with the Vector Spectromagnetograph instrument (VSM) on the *Synoptic Optical Long-term Investigations of the Sun telescope* (SOLIS) (Keller, Harvey, and Giampapa, 2003) and the *Helioseismic and Magnetic Imager* (HMI) (Schou et al., 2012; Scherrer et al., 2012) aboard the *Solar Dynamics Observatory* (SDO) (Pesnell, Thompson, and Chamberlin, 2012) after May 2010. Full disk vector magnetograms not only provide key observations to capture the entire process of dynamic emergence, evolution and decay of active regions, but also allow the production of synoptic maps using vector magnetic field data (Gosain et al., 2013; Liu et al., 2017). These synoptic maps provide vector magnetic fields measured over the entire Sun's surface, once per rotation, and thus are essential for many space weather models, such as solar wind prediction models.

Recently a systematic bias in full disk magnetograms was reported (Pevtsov et al., 2021). It was found that the east–west component of the magnetic field,  $B_\phi$  or  $B_p$ , in low polarization signal areas (i.e. weak field or quiet regions) changes its sign after the regions cross the central meridian. This hemispheric bias is seen in both VSM/SOLIS and HMI/SDO magnetograms (Virtanen, Pevtsov, and Mursula, 2019; Pevtsov et al., 2021). Pevtsov et al. (2021) suggest that the different noise levels between the measured longitudinal and transverse field components, together with the filling factor and disambiguation, is the reason for this bias.

Although this bias only occurs in weak field regions, it inevitably yields incorrect data and thus has the potential to impact various research such as data-driven numerical models and simulations. Our goal is to understand what causes this bias and search for possible solutions to remove it. In this study, we report the possible reason causing the bias and a method to resolve it. The paper is organized as follows. In Section 2, we describe the hemispheric bias. A diagnosis of the cause is given in Section 3. We present our solution to the problem in Section 4. The work is summarized in Section 5.

## 2. Hemispheric Bias in Vector Magnetic Field Measurements

The HMI instrument is a filtergraph with a full disk coverage of  $4096 \times 4096$  pixels. The spatial resolution is about  $1''$  with a  $0.5''$  pixel size. The width of the filter profiles is  $76 \text{ m}\text{\AA}$ . The spectral line is the Fe I 6173  $\text{\AA}$  absorption line formed in the photosphere (Norton et al., 2006). There are two CCD cameras in the instrument, the “front camera” and the “side camera”. The front camera acquires the filtergrams at 6 wavelengths along the line Fe I 6173  $\text{\AA}$  in two polarization states with 3.75 seconds between images. It takes 45 seconds to acquire a set of 12 filtergrams. This set of data is used to derive the Dopplergrams and the line-of-sight magnetograms. The side camera is dedicated to measuring the vector magnetic field. It takes 135 seconds to obtain the filtergrams in 6 polarization states at 6 wavelength positions. After April 2016, the observation mode changed and the side camera only takes linear polarization states at 6 wavelengths in 90 seconds, and vector magnetic field is then derived from a combination of the measurements from both cameras. The Stokes parameters [I, Q, U, V] are computed from these measurements and further inverted to retrieve the vector magnetic field. In order to suppress the p-modes and increase the signal-to-noise ratio, usually the Stokes parameters are derived from the filtergrams averaged over a certain time. Currently, the average is taken from 720-second measurements. They are then inverted to produce the vector magnetic field using an inversion algorithm Very Fast Inversion of the Stokes Vector

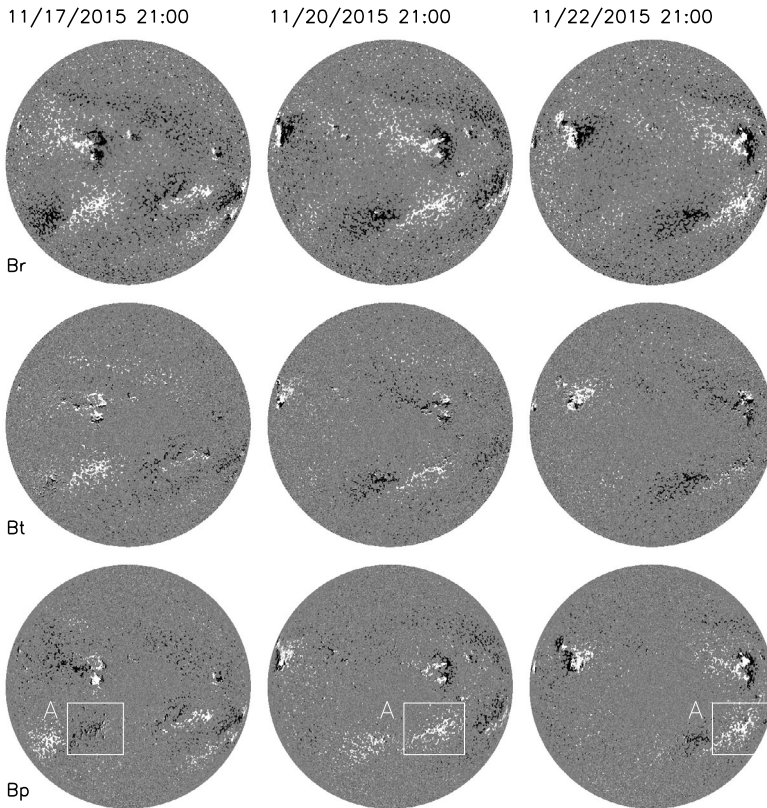


**Figure 1** Full disk vector magnetograms taken by the HMI. From top to bottom:  $B_r$  (radial field),  $B_t$  (north-south component), and  $B_p$  (east-west component). From left to right are data taken on 2015 November 17, 20 and 22, respectively. The plots are saturated at  $\pm 60 \text{ Mx cm}^{-2}$ . Region A marks a weak field region in which  $B_p$  changes sign after crossing the central meridian. The solar north points upward. The positive (negative) field is white (black).

(VFISV). VFISV is a Milne-Eddington (ME) based approach developed at the High Altitude Observatory (HAO) (Borrero et al., 2011; Centeno et al., 2014). The  $180^\circ$  degree ambiguity of the azimuth is resolved based on the “minimum energy” algorithm (Metcalf, 1994; Leka et al., 2009). In this paper, all magnetic fields and their components mentioned refer to the flux density with the unit  $\text{Mx cm}^{-2}$ , except for the field from simulation data.

As stated in Section 1, the full disk vector magnetograms show a hemispheric bias with the  $B_p$  in weak field regions changing its sign after crossing the central meridian (Pevtsov et al., 2021). We show in Figure 1 an example of the hemispheric bias with HMI vector magnetograms. A weak field region marked “A”, rotates from the eastern to the western hemisphere in this 5-day period. The east-west component of the magnetic field,  $B_p$ , in the leading magnetic patch is negative at the beginning on November 17, and changes to positive on November 20 and 22, after the region crosses the central meridian; the following patch has positive  $B_p$  on November 17 and 20, and changes to negative on November 22 after it crosses the central meridian. The signs of the other two components,  $B_r$  and  $B_t$ , basically remain unchanged.

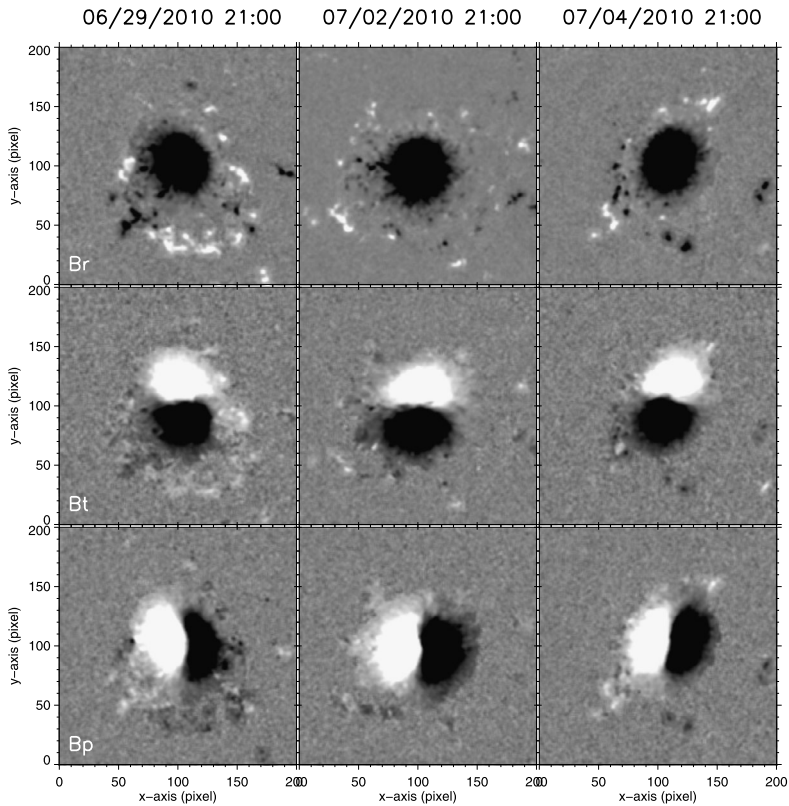


**Figure 2** Vector magnetograms for the active region AR 11084 during its disk passage. From top to bottom:  $B_r$ ,  $B_t$ , and  $B_p$ ; from left to right: 2010 June 29, July 2, and July 4. The positive (negative) field is white (black). The fields are saturated at  $\pm 300 \text{ Mx cm}^{-2}$ .

This bias does not occur in strong field regions in sunspots. Shown in Figure 2 are the magnetic field of an active region, AR 11084, from 2010 June 29 to July 4. During this 5-day period, AR 11084 rotates from the eastern hemisphere to the west. The signs of the three components do not change in the central active region after the region crosses the central meridian.

### 3. Reasons for the Hemispheric Bias

For solar magnetic field observations, the Zeeman effect is usually used to measure the line-of-sight (circular polarization) and transverse (linear polarization) components of vector magnetic field. For the magnetic field vector in spherical coordinates, radial ( $B_r$ ), theta ( $B_\theta$  or  $B_t$ ) and phi ( $B_p$ ), each component is contributed from observed line-of-sight (los) and transverse fields. When mismatch between los and transverse fields happens, the sign of the component follows the dominant field.

Incorrectly determining the filling factor for structures in magnetograms can lead to this mismatch. In the weak-field approximation (Jefferies and Mickey, 1991), the inclination of

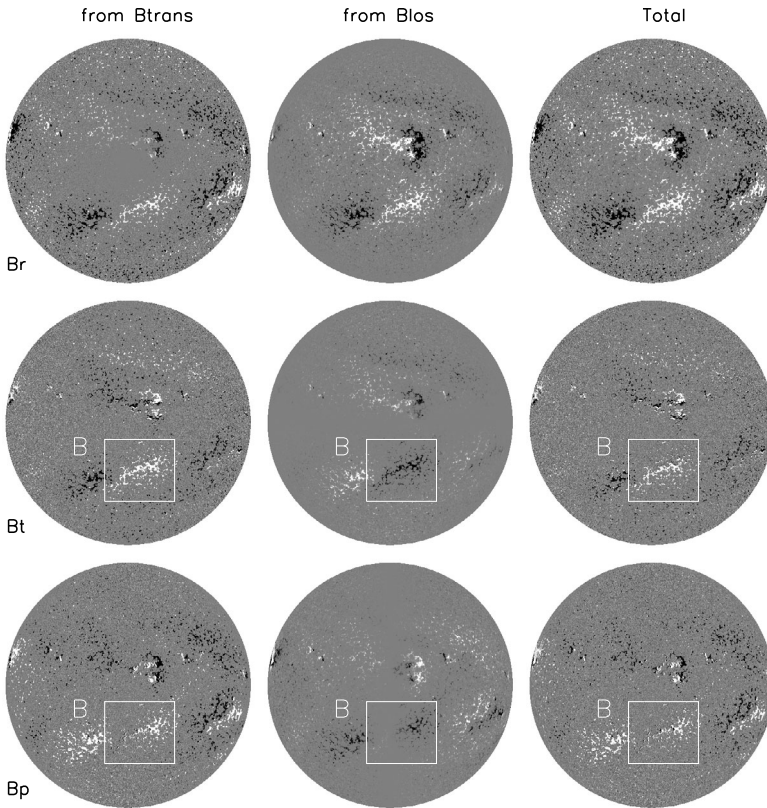


**Figure 3** Full disk vector magnetograms from HMI taken at 21:00 UT on 2015 November 19. From top to bottom:  $B_r$ ,  $B_t$ , and  $B_p$ ; from left to right: the field component from the transverse ( $B_p^{trans}$ ), the line-of-sight ( $B_p^{los}$ ), and the sum of both, respectively. The positive (negative) field is white (black). The field is saturated at  $\pm 60.0 \text{ Mx cm}^{-2}$ .

vector magnetic field  $\mathbf{B}$ ,  $\gamma$ , depends on the Stokes parameters ( $Q, U, V$ ) as

$$\tan \gamma \propto \alpha^{1/2} \frac{(Q^2 + U^2)^{1/4}}{V}, \tag{1}$$

where  $\alpha$  is the filling factor. In the inversion procedure used to-date to derive the HMI vector magnetograms, the filling factor was set to be unity. It is close to the true value in the sunspot umbrae and penumbrae, but much greater than the solar value for the quiet-Sun regions. The transverse field is therefore over-estimated in these regions.

The contributions to  $B_p$  ( $B_t$  as well) from the line-of-sight field,  $B_p^{los}$  ( $B_t^{los}$ ), and the transverse field,  $B_p^{trans}$  ( $B_t^{trans}$ ), are found to have opposite signs in weak field regions. Figure 3 shows the  $B_r$  (top),  $B_t$  (middle), and  $B_p$  (bottom) for the transverse (left) and line-of-sight (middle) fields separately. The right column shows the sum of the two contributions from transverse and line-of-sight fields. For weak field regions, the contributions from two components to  $B_p$  and  $B_t$  are basically of opposite sign. For example, the signs of  $B_p^{trans}$  and  $B_p^{los}$  and the signs of  $B_t^{trans}$  and  $B_t^{los}$  in the region “B” are opposite. Also, the sum of the two

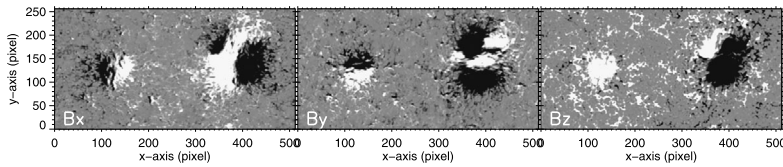


**Figure 4** Vector magnetic field data from simulations (Cheung et al., 2019). From left to right:  $B_x$ ,  $B_y$ , and  $B_z$ . The plots are saturated at  $\pm 200.0 \text{ Mx cm}^{-2}$ .

contributions has the same sign as that of the transverse field. Because  $B_p^{los}$  in weak field regions changes sign after crossing the central meridian, the sign of  $B_p^{trans}$  changes as well.

Thus, it is shown that in weak field regions  $B_p^{trans}$  and  $B_p^{los}$  have opposite signs. So do  $B_t^{trans}$  and  $B_t^{los}$ . If the line-of-sight or transverse field is over-estimated or under-estimated systematically, i.e. a mismatch exists between the line-of-sight and transverse fields, this leads to sign differences in  $B_p$  between the two hemispheres, following the sign of the dominant one between the line-of-sight and transverse fields. In the HMI measurement, the signs of  $B_p$  and  $B_t$  follow the contributions from the transverse fields.

It is unlikely that disambiguation for transverse fields causes the hemispheric bias problem. For example, suppose we choose the other solution of disambiguation for the weak field in the western hemisphere. This solves the bias problem in  $B_p$ , i.e.  $B_p$  remains unchanged in sign from the eastern hemisphere to the west. However, it leads to a sign change in the  $B_t$  component between the two hemispheres.

We examine this bias problem with simulation data from Cheung et al. (2019). This is an active region simulation. The data includes a sunspot group on the right hand side area with fields of both polarities, a sunspot on the left hand side with positive field, and weak fields in between and outside the sunspot regions as well (see Figure 4). To be consistent with the HMI magnetograms, positive  $B_y$  points downwards. Because the data are from simulations, it does not have the mismatch problem.

We place the data in four quadrants and simulate the HMI pipeline processing. The vector field data are placed in north  $15^\circ$  east  $30^\circ$  (N15E30), S15E30, N15W30, and S15W30, respectively. The pixel size of the simulated data is roughly 600 km. First, we map the vector field data to the Sun's surface on the image coordinates, similar to the HMI full-disk magnetograms; we then transfer the three components of the vector field  $B_x$ ,  $B_y$ , and  $B_z$  to the field strength, inclination and azimuth; finally we add  $180^\circ$  ambiguity in azimuth. Now we have a full disk vector magnetic field similar to HMI vector magnetograms after the inversion (Pseudo-HMI magnetograms hereafter).

This pseudo-HMI magnetogram data is processed through the HMI pipeline for disambiguation. The results are shown in Figure 5. Basically, the vector field data in all four quadrants are similar to the original data as shown in Figure 4.  $B_r$ ,  $B_t$ , and  $B_p$  in the sunspot group, sunspot, and quiet-Sun regions do not show the hemispheric bias problem. The panels in the third row in Figure 7, which display  $B_p$  and  $B_t$  in the N15E30 and N15W30 regions, show this in more detail.

We further examine the contributions of the line-of-sight and transverse fields, respectively. Figure 6 shows the contributions to  $B_p$  (top) and  $B_t$  (bottom) of transverse (left,  $B_p^{trans}$  and  $B_t^{trans}$ ) and line-of-sight (middle,  $B_p^{los}$  and  $B_t^{los}$ ) fields for the region at N15E30, as shown in Figure 5. The right panels are the sum of  $B_p$  and  $B_t$  from both transverse and line-of-sight fields. Here we analyze three areas in the region: the sunspot group on the right area, the sunspot on the left area, and the quiet-Sun (weak field) area in the middle, between the sunspot group and the sunspot.  $B_x$ ,  $B_y$ , and  $B_z$  in the sunspot group, as shown in

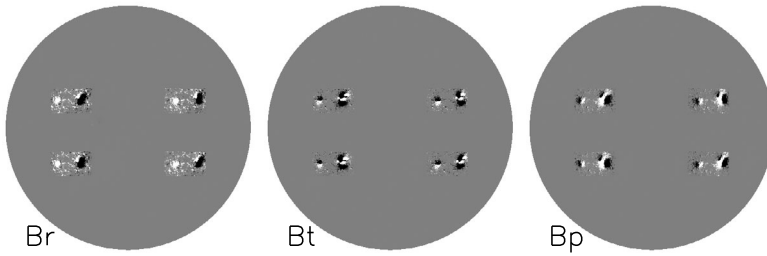


**Figure 5** Pseudo-HMI vector magnetograms from simulated data of the vector magnetic field placed in four quadrants at N15E30, S15E30, N15W30 and S15S30, respectively. The simulated data are from Cheung et al. (2019), as shown in Figure 4. The plots are saturated at  $\pm 200 \text{ Mx cm}^{-2}$ .

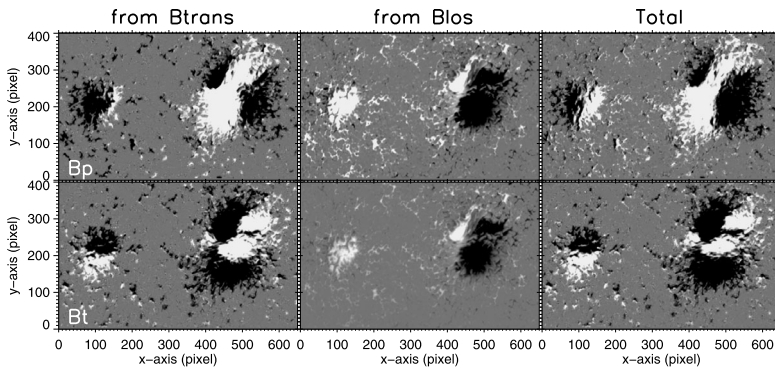


**Figure 6** A breakdown of  $B_p$  (top) and  $B_t$  (bottom) from transverse (left,  $B_p^{trans}$  and  $B_t^{trans}$ ) and line-of-sight (middle,  $B_p^{los}$  and  $B_t^{los}$ ) fields for the region at N15E30, as shown in Figure 5. Right panels show the total of  $B_p$  and  $B_t$  from both transverse and line-of-sight fields. The plots are saturated at  $\pm 200 \text{ Mx cm}^{-2}$ .

Figure 4, suggest local magnetic connectivity between the two magnetic patches with opposite signs of  $B_z$ . In this region,  $B_p^{los}$  has two patches: one big negative patch and one small positive patch. The negative patch has both positive and negative  $B_p^{trans}$ , indicating that  $B_p^{los}$  and  $B_p^{trans}$  can have the same sign in some areas. The sign of the total  $B_p$  is not exactly the same as either of them, but rather a combination of the two. For the sunspot region,  $B_p^{los}$  is positive.  $B_p^{trans}$  is negative in a big patch of the region and positive in a small patch. So, for most pixels,  $B_p^{los}$  and  $B_p^{trans}$  are opposite in sign. Total  $B_p$  is positive and negative roughly equally in the region, indicating neither  $B_p^{los}$  nor  $B_p^{trans}$  is dominant. In the quiet-Sun region, the signs of  $B_p^{los}$  and  $B_p^{trans}$  are basically opposite. The sign of total  $B_p$  is mixed. Again, this suggests that neither  $B_p^{los}$  nor  $B_p^{trans}$  is dominant in this region. Thus, depending on the magnetic configuration, the sign of  $B_p^{los}$  and  $B_p^{trans}$  can be the same. If the data do not have the mismatch problem between the line-of-sight and transverse fields, the sign of  $B_p$  is not determined solely by one of the two fields, but rather a combination of both.

We test the impact of the mismatch between the line-of-sight and transverse fields in regards to the hemispheric bias. For the pseudo-HMI vector magnetograms, we adjust the inclination by either increasing or decreasing the inclination by a factor of 30% of its original value to produce two additional pseudo-HMI vector magnetograms. Therefore, in one magnetogram, the transverse field is systematically over-estimated (*over-case* hereafter); in

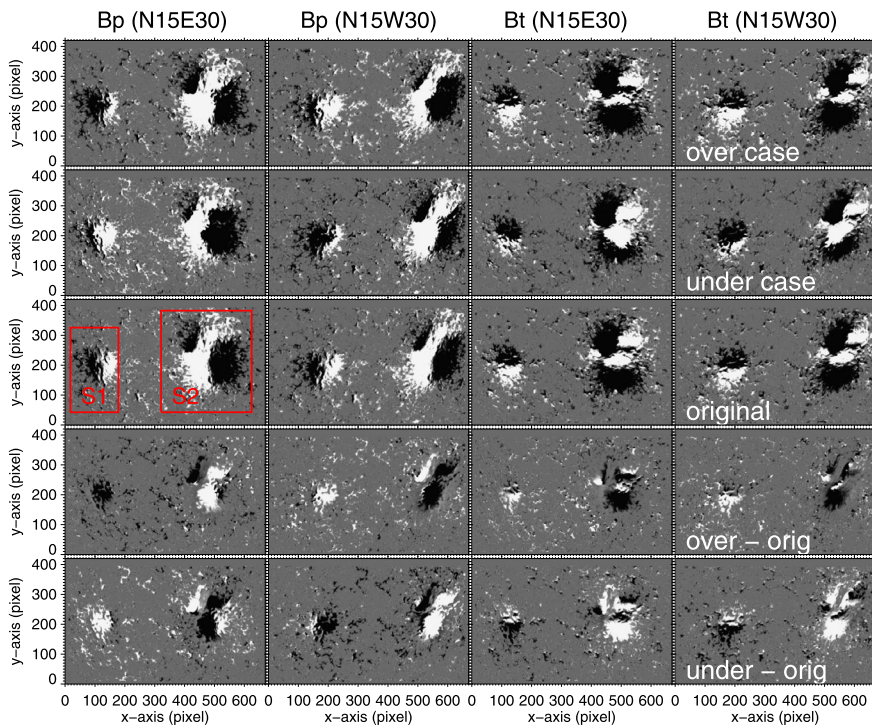


**Figure 7** Magnetic fields  $B_p$  (the first two columns) and  $B_t$  (the third and fourth columns) for two regions on the solar disk from three pseudo-HMI magnetograms. Magnetic fields in the north-east (N15E30) solar region are shown in columns 1 and 3; the north-west (N15W30) region are in columns 2 and 4. From top to bottom are data from the over-estimated case (top row), the under-estimated case (second), the original data (third), the difference between the *over-case* and original data (fourth), and the difference between the *under-case* and the original (bottom), respectively. The plots are saturated at  $\pm 200 \text{ Mx cm}^{-2}$ .

the other, the transverse field is under-estimated (*under-case* hereafter). The two pseudo-HMI magnetograms are then processed through the HMI pipeline to solve the ambiguity. The disambiguated magnetograms are shown in Figure 7. We only show the N15E30 (first and third columns) and N15W30 (second and fourth columns) regions for  $B_p$  (first and second columns) and  $B_t$  (third and fourth columns) fields. The first and second rows are data from the *over-case* and *under-case*. The third row shows the no-mismatch data (original data hereafter, see Figure 5). The fourth and fifth rows show the differences between the *over-case* and the original data (fourth row), and between the *under-case* and the original data (fifth row), respectively. For the sunspot and sunspot group in the region enclosed by the rectangles marked “S1” and “S2” in the column 1 and row 3 panel, many pixels change their sign for  $B_p$  from the eastern hemisphere to the western for both *over-case* and *under-case*. The sign-changed pixels are easily seen in the difference plots shown in the fourth and fifth rows. Most pixels in the quiet-Sun regions change signs. For example, in the quiet region in the middle between the sunspot (the “S1” area) and the sunspot group (the “S2” area),  $B_p$  changes sign from negative to positive for the *over-case* and from positive to negative for the *under-case*.  $B_t$  for both cases does not change the sign. This test suggests that (i) a mismatch between the observed line-of-sight and the transverse fields can cause the hemispheric bias, and (ii) strong fields with local magnetic connectivity may minimize this bias: The sign of



$B_p$  in some pixels in the sunspot (area “S1”) and sunspot group (area “S2”) does not change between the eastern and western hemispheres.

#### 4. One Solution for the Hemispheric Bias Problem

To solve this bias, Grifón-Marín et al. (2021) have improved the inversion algorithm and the filling factor can be derived from the updated VFISV. Shown in Figure 8 are  $B_p$  in the quiet-Sun region “A” (see Figure 1) for a time period of 5 days from 2015 November 17 to 21, when the region rotated from the eastern hemisphere to the west. The data are from the updated VFISV (right panels) and the original VFISV (right). The data are mapped to spherical coordinates to avoid projection effects. The sign changes from the eastern to the western hemisphere when the filling factor is set to a constant of unity (right panels). This hemispheric bias has been mitigated substantially when the filling factor is not set to unity but inverted as a variable (left).

More quantitatively, we show in Figure 9 the percentage of pixels in region “A” that have  $B_p < 0$  for the 5-day period. Only the pixels with a field strength greater than  $300 \text{ Mx cm}^{-2}$ ,  $3\sigma$  of the HMI vector data (Hoeksema et al., 2014), are included. The percentage for the original data shows a significant hemispheric bias that changes from 84.8% in the eastern hemisphere to 3.2% in the western (the red dots in Figure 9). In contrast, it is 44.3% in the eastern hemisphere and 33.9% in the western for the new data (black dots). The updated VFISV mitigates the hemispheric bias significantly.

We compare 2015 November 17 17:12 UT vector magnetograms derived by the original and updated VFISV. About 24% of the pixels with a field greater than the noise level (roughly  $100 \text{ Mx cm}^{-2}$ ) have opposite signs in  $B_p$ . If the updated VFISV produces the true magnetic field data, this indicates that 24% of the pixels in the original vector magnetograms have a wrong sign in  $B_p$ .

Vector magnetic field on the spheric coordinates,  $B_r$ ,  $B_t$ , and  $B_p$ , is contributed from the observed line-of-sight and transverse fields.  $B_r$  may be impacted by this mismatch, as well. Shown in Figure 10 is average of  $\delta B_r$ , the difference of  $B_r$  between the new and original data, over 15 days. Here  $\delta B_r = |B_r^{old}| - |B_r^{new}|$ . The average is calculated for the data from 2015 November 15 to 30, with a cadence of 3 hours. Only the pixels with  $B > 300.0 \text{ Mx cm}^{-2}$  are included for averaging. If  $B_r^{new}$  is ground true,  $B_r^{old}$  is generally over-estimated, and this over-estimation increases towards the limb.  $\delta B_r$  is slightly higher in the eastern hemisphere than in the western hemisphere, indicating that  $B_r^{old}$  may also have a hemispheric bias.

Figure 11 shows normalized histograms of the average  $\delta B_r$  (see Figure 10) for 10 rectangular regions in the eastern and western hemisphere. The size of the regions is  $200 \times 1945$  pixels<sup>2</sup>, centered at  $[\pm 0.4R_s, Y_c]$ ,  $[\pm 0.5R_s, Y_c]$ ,  $[\pm 0.6R_s, Y_c]$ ,  $[\pm 0.7R_s, Y_c]$ , and  $[\pm 0.8R_s, Y_c]$ , where  $R_s$  is the solar radius and  $Y_c$  is disk center on the Y-axis. The solid (dashed) lines refer to the regions in the eastern (western) hemisphere. It can be seen that  $B_r^{old}$  is over-estimated. We further fit the histograms with a Gaussian function. The peaks of the Gaussian are shown in Figure 12. The peaks from the regions in the eastern hemisphere are slightly greater than those from the western hemisphere, suggesting that  $B_r$  has a hemispheric bias problem as well.

This mismatch not only leads to a wrong sign of  $B_p$  in weak field regions, but also impacts  $B_r$  that is widely used in many models, such as solar wind speed prediction model. The updated VFISV can mitigate this mismatch. It is also found that the updated VFISV minimizes an apparent bias in the polar field. The polar field vectors in the original HMI

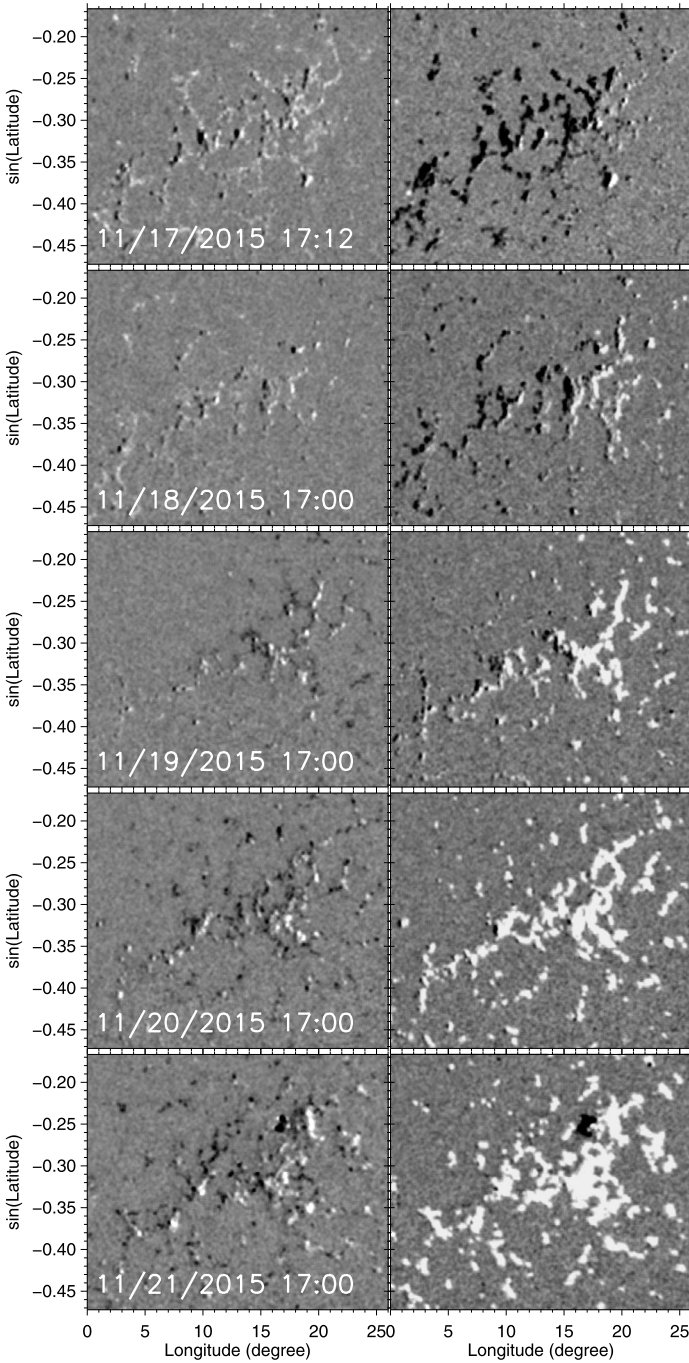


**Figure 8**  $B_p$  is shown from region “A”, as shown in Figure 1, for a time period of 5 days when the region rotates from the eastern to the western hemisphere. The data are inverted with the updated VFISV (left) with the filling factor as a variable and by the original VFISV code (right) with a filling factor of unity. The data are mapped to the Carrington coordinates to avoid any foreshortening effect. The plots are saturated at  $\pm 80 \text{ Mx cm}^{-2}$ .

**Figure 9** The percentage of pixels with  $B_p < 0$  in region “A”, as shown in Figure 8, for a time period of 5 days when the region rotates from the eastern to the western hemisphere. The black (red) dots refer to the data from the updated (original) VFISV. The error bars refer to a confidence interval with a 99% confidence level. Only the pixels with field strengths greater than  $300 \text{ Mx cm}^{-2}$ ,  $3\sigma$  of the data (Hoeksema et al., 2014), are included.

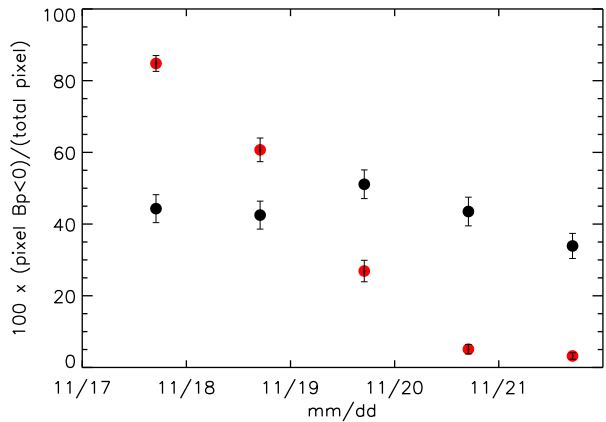
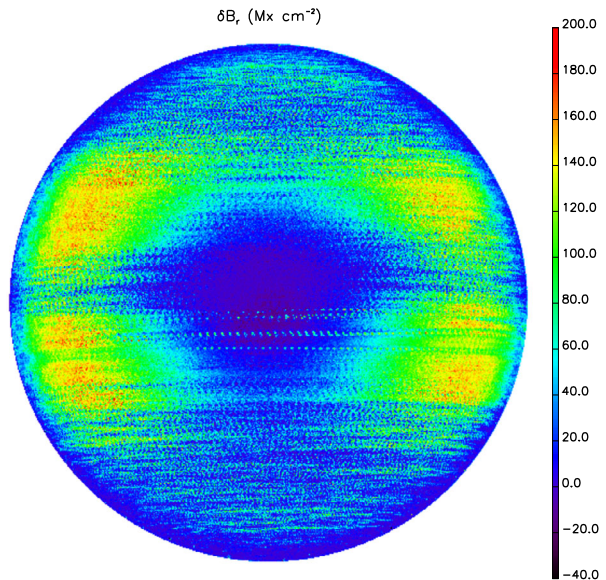


**Figure 10** Average of  $\delta B_r$  over 15 days.  $\delta B_r = |B_r^{old}| - |B_r^{new}|$ . Only the pixels with  $B > 300.0 \text{ Mx cm}^{-2}$  are included for averaging.



data are more inclined toward the plane of the sky compared to the local radial vectors, leading to a systematic tilt towards the pole (Sun et al., 2021). The effect may be explained by the unresolved field structures. Indeed, the field vectors become more radial after the filling factor has been taken into account.

It is interesting to note that a similar poleward tilted pattern in the polar fields was measured at Mount Wilson Observatory, based on a correction required to minimize annual variations in the radial field derived from line-of-sight observations (Ulrich and Tran, 2013). On the other hand, the polar field vectors from SOLIS/VSM appear to systematically tilt towards the equator (Gosain et al., 2013; Virtanen, Pevtsov, and Mursula, 2019).

Using the updated VFISV code is computationally expensive. For a nominal full disk magnetogram, computing time is about 5 times that of using the original code. Applying the new code to selected pixels may be one solution to reduce the computing time. For example, processing the pixels with a total polarization signal greater than 0.25% (Griñón-Marín et al.,

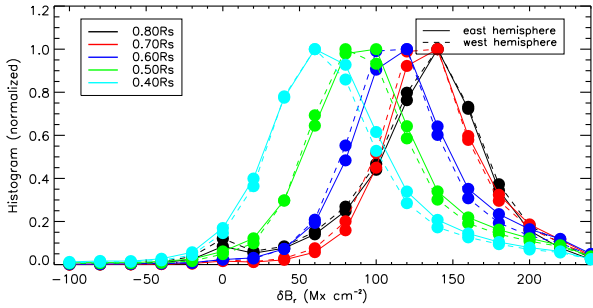
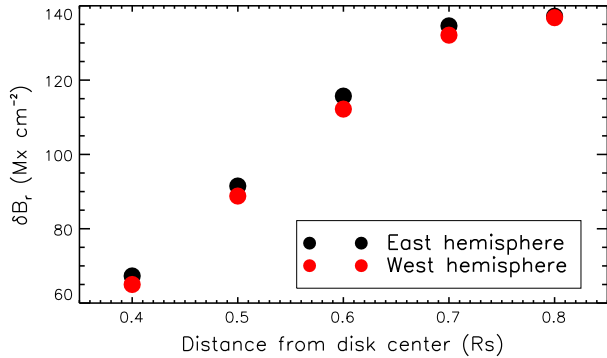


**Figure 11** Normalized histograms of  $\delta B_r$  for 10 rectangular regions in the eastern and western hemispheres. Colors refer to regions centered at  $[\pm 0.4R_s, Y_c]$ ,  $[\pm 0.5R_s, Y_c]$ ,  $[\pm 0.6R_s, Y_c]$ ,  $[\pm 0.7R_s, Y_c]$ , and  $[\pm 0.8R_s, Y_c]$ , respectively.  $Y_c$  refers to the disk center. The size of the regions is 200 pixels  $\times$  1945 pixels. The solid and dashed lines represent regions in the eastern and western hemisphere, respectively.

**Figure 12** Shift of peaks of a Gaussian function that fits the distribution of  $\delta B_r$  as shown in Figure 11.



2021) reduces the computing time substantially to 1.6 times that of the original one, while the effect is comparable to that when the new code is applied to all pixels: The pixels with opposite signs in  $B_p$  between the original and the new data are 24% when the code is applied to all pixels, compared to 22% when it is applied to the pixels with a polarization signal greater than 0.25%.

### 5. Conclusion

In this paper we present a study of the hemispheric bias problem in full disk vector magnetograms. It is shown that the  $B_p$  component (east-west component) of the magnetic field in regions with low polarization signal (weak field) changes its sign after the regions have crossed the central meridian. This problem is caused by a mismatch between line-of-sight and transverse fields during measurement and calibration. For HMI vector magnetograms, this mismatch is caused by the handling of the filling factor during the inversion procedure. Currently the filling factor is set to be unity everywhere on the Sun’s surface, which is much greater than the true solar value of the filling factor in the quiet-Sun regions. For a nominal full disk vector magnetogram, about 24% of the pixels with a meaningful polarization signal may suffer from this hemispheric bias problem. Consequently, vector magnetic field at these pixels may not be precisely determined.

Recently, the inversion algorithm used for HMI data processing has been improved to derive the filling factor (Griñón-Marín et al., 2021). It is shown that the improved algorithm mitigates the hemispheric bias substantially.

**Acknowledgments** The authors would like to thank the anonymous referee for valuable suggestions and comments that helped improve the paper. This work was supported by NASA Contract NAS5-02139 (HMI) to Stanford University. X. Sun acknowledges support from NASA award 80NSSC21K0736. ABGM acknowledges support from the Research Council of Norway through its Centres of Excellence Scheme, Project Number 262622. The data have been used by courtesy of NASA/SDO and the HMI science team.

**Data Availability** The datasets generated during and/or analyzed during the current study are available from the corresponding author on reasonable request.

## Declarations

**Disclosure of Potential Conflicts of Interest** The authors declare that they have no conflicts of interest.

## References

- Borrero, J.M., Tomczyk, S., Kubo, M., Socas-Navarro, H., Schou, J., Couvidat, S., Bogart, R.: 2011, *Solar Phys.* **273**, 267. DOI.
- Centeno, R., Schou, J., Hayashi, K., Norton, A., Hoeksema, J.T., Liu, Y., Leka, K.D., Barnes, G.: 2014, *Solar Phys.* **289**, 3531. DOI.
- Cheung, M.C.M., Rempel, M., Chintzoglou, G., Chen, F., Testa, P., Martínez-Sykora, J., et al.: 2019, *Nat. Astron.* **3**, 160. DOI.
- Gosain, S., Pevtsov, A.A., Rudenko, G.V., Anfinogentov, S.A.: 2013, *Astrophys. J.* **772**, 52. DOI.
- Griñón-Marín, A.B., Yabar, A.P., Liu, Y., Hoeksema, J.T., Norton, A.: 2021, *Astrophys. J.* **923**, 84. DOI.
- Hoeksema, J.T., Liu, Y., Hayashi, K., Sun, X., Schou, J., Couvidat, S., et al.: 2014, *Solar Phys.* **289**, 3483. DOI.
- Jefferies, J.T., Mickey, D.L.: 1991, *Astrophys. J.* **372**, 694. DOI.
- Keller, C.U., Harvey, J.W., Giampapa, M.S.: 2003, In: Keil, S.L., Avakyan, S.V. (eds.) *Innovative Telescopes and Instrumentation for Solar Astrophysics, Society of Photo-Optical Instrumentation Engineers (SPIE) Conference Series* **4853**, 194.
- Leka, K.D., Barnes, G., Crouch, A.D., Metcalf, T.R., Gary, G.A., Jing, J., Liu, Y.: 2009, *Solar Phys.* **260**, 83. DOI.
- Liu, Y., Hoeksema, J.T., Sun, X., Hayashi, K.: 2017, *Solar Phys.* **292**, 29. DOI.
- Metcalf, T.R.: 1994, *Solar Phys.* **155**, 235. DOI.
- Norton, A.A., Graham, J.P., Ulrich, R.K., Schou, J., Tomczyk, S., Liu, Y., et al.: 2006, *Solar Phys.* **239**, 69. DOI.
- Pesnell, W.D., Thompson, B.J., Chamberlin, P.C.: 2012, *Solar Phys.* **275**, 3. DOI.
- Pevtsov, A.A., Liu, Y., Virtanen, I., Bertello, L., Mursula, K., Leka, K.D., Hughes, A.L.H.: 2021, *J. Space Weather Space Clim.* **11**, 14. DOI.
- Scherrer, P.H., Schou, J., Bush, R.I., Kosovichev, A.G., Bogart, R.S., Hoeksema, J.T., et al.: 2012, *Solar Phys.* **275**, 207. DOI.
- Schou, J., Scherrer, P.H., Bush, R.I., Wachter, R., Couvidat, S., Rabello-Soares, M.C., et al.: 2012, *Solar Phys.* **275**, 229. DOI.
- Sun, X., Liu, Y., Milić, I., Griñón-Marín, A.B.: 2021, *Res. Notes Am. Astron. Soc.* **5**, 134. DOI.
- Ulrich, R.K., Tran, T.: 2013, *Astrophys. J.* **768**, 189. DOI.
- Virtanen, I.I., Pevtsov, A.A., Mursula, K.: 2019, *Astron. Astrophys.* **624**, A73. DOI.

**Publisher's Note** Springer Nature remains neutral with regard to jurisdictional claims in published maps and institutional affiliations.